THE ASTROPHYSICAL JOURNAL, 428:555–573, 1994 June 20

ROSAT PSPC OBSERVATIONS OF NGC 4636: INTERACTION WITH VIRGO GAS?

G. TRINCHIERI
Osservatorio Astrofisico di Arcetri[1] and Harvard-Smithsonian Center for Astrophysics[2]
D.-W. KIM
Chungnam National University,[3] and Harvard-Smithsonian Center for Astrophysics[2]
G. FABBIANO
Harvard-Smithsonian Center for Astrophysics[2]
AND
C. R. C. CANIZARES
MIT[4]
Received 1993 August 30; accepted 1993 December 17

ABSTRACT

ROSAT PSPC observations of NGC 4636 have provided a deep image of the galaxy and its surroundings, which reveal the presence of emission well outside the optical galaxy. The source emission is measured out to $r \sim 18'$, where the instrument support structure prevents us at this time from following it farther out. The nature of this emission is not fully understood, but could be evidence that the Virgo cluster gas extends as far out as this galaxy (>3 Mpc from M87).

Spectral analysis of the X-ray emission suggests a relatively cool ($kT \sim 0.5$–0.9 keV) interstellar medium, with temperatures increasing with radius. However, the detailed properties of the interstellar gas cannot be unambiguously determined with the present data, since the results we obtain depend strongly on the choice of the spectral model. Comparison of the spectral distributions in concentric annuli clearly indicates significant differences with radius, which can be parameterized as a general increase of the temperature. For low cosmic abundance models, kT varies from ~ 0.55 keV in the inner $1'$ to ~ 0.8 keV at $r \sim 6'$–$8'$. Outside $8'$ the average temperature is higher than in the inner region ($kT \sim 0.8$–1.2 keV) and the low-energy absorption is significantly lower. For 100% cosmic abundance and galactic line-of-sight absorption, multi-temperature fits are required, suggesting the possibility that the interstellar medium is inhomogeneous.

Subject headings: galaxies: clusters: individual (Virgo) — galaxies: individual (NGC 4636) — galaxies: ISM — X-rays: galaxies

1. INTRODUCTION

Early *Einstein* observations of normal galaxies in the Virgo cluster have suggested that the emission of the brightest ellipticals could be attributed to the presence of hot gas radiating at $kT \sim 1$ keV (Forman et al. 1979; Trinchieri, Fabbiano, & Canizares hereafter TFC). Both the high X-ray luminosities and the soft spectra observed in the X-ray bright early-type galaxies have indicated the presence of an interstellar medium in these objects, previously thought to be devoid of gas (see Fabbiano 1989 and references therein).

This discovery has provided a potentially powerful tool for estimating galaxy masses (M) out to radii well outside the central regions, to which optical spectroscopic data have generally been restricted, and has led to the suggestion that large amounts of dark matter are a common feature of early-type systems (Forman, Jones, & Tucker 1985; Fabian et al. 1986). However, the combined spatial and spectral resolution of the *Einstein* X-ray data was not sufficient to yield an unequivocal determination of the masses in early-type galaxies (see TFC). In principle X-ray data could determine the temperature at each radius, and in particular at large radii where mass measurements are more interesting. Instead, only a gas temperature averaged over the entire source could be derived with the *Einstein* data, and even this mean depended on the assumption of a given (solar) metal abundance. Only estimates of radial temperature distributions have been attempted in a few cases (see Forman et al. 1985). Improved measurements are important. For example, a radially increasing temperature could indicate the presence of an external pressure and consequently relax the need for dark matter to confine the hot interstellar medium (e.g., Cowie & Binney 1977; Vedder, Trester, & Canizares 1988; Bertin, Pignatelli, & Saglia 1993).

Moreover the determination of the radial extent of the gas and to a lesser degree of the density gradient at large radii are also uncertain. In particular, in the observations of NGC 4636, emission observed at galactocentric radii of $\sim 6'$–$7'$ could have been due to an instrumental feature, and thus could not be unambiguously attributed to the source. In other cases, contamination from the emission of unconnected sources in the field could not be discarded. These uncertainties reflect directly in the evaluation of M.

To address this issue, deep observations of some of the more luminous galaxies have been obtained with the PSPC (Position Sensitive Proportional Counter) aboard the *ROSAT* satellite (Truemper 1983; Pfeffermann et al. 1987). The *ROSAT* band (~ 0.1–2 keV) is softer than the *Einstein* band (~ 0.2–3.5 keV), and the PSPC is more sensitive than the *Einstein* IPC and has better energy and angular resolutions. Moreover, longer obser-

[1] Currently at the Osservatorio Astronomico di Brera Via Brera 28, 20121 Milano, Italy.
[2] 60 Garden St., Cambridge, MA 02138.
[3] Department of Astronomy and Space Science, 305-764, Daejeon, South Korea.
[4] Center for Space Research, Cambridge, MA 02139.

vations have been obtained, to achieve a greater sensitivity. We report here the results obtained for NGC 4636, at the outskirts of the Virgo cluster, one of the brightest early-type galaxies, and one of the best examples selected to study the emission at large radii and to derive accurately gas properties and the total gravitational mass.

NGC 4636 was chosen because it is believed to be a relatively isolated object (albeit at the edge of the Virgo cluster), with an X-ray flux $f_X \sim 10^{11}$ ergs s^{-1} cm^{-2} measured by *Einstein*, or $L_X \sim 3.5 \times 10^{41}$ ergs s^{-1} for $D = 17$ Mpc (Tully 1988). In the optical, it is classified as E.0+, with $m_B = 10.43$, $R_e \sim 90''$ and $R_{25} \sim 300''$ (RC3).

2. DATA ANALYSIS

NGC 4636 was observed by the *ROSAT* PSPC in 1991 December, for a total livetime of ~13,000 s. The observation was carried out without any spectral filters in the field of view, to take advantage of the full spectral coverage of *ROSAT*.

The X-ray data analysis is based on the routines available in the "xray" software package (PROS) running under IRAF, and on the XSPEC spectral package.

2.1. *Source Extent*

The grayscale, raw PSPC image of NGC 4636 is shown in Figure 1. The emission is clearly peaked at the target position, but other features are also present. In spite of the fact that there is no correction for uneven exposure and vignetting effects, a clearly extended, low surface brightness component is visible, inside the typical "wagon wheel" PSPC support structure, with a few sources embedded in it. Fainter sources are also visible at large radii. All of the individual sources will be excluded from the present analysis of the NGC 4636 emission, by masking them out with circles of 2′–4′ radius (to take into account the vignetting and point-spread function effects at large off-axis angles). However, it should be noted that their inclusion in the analysis does not alter the results.

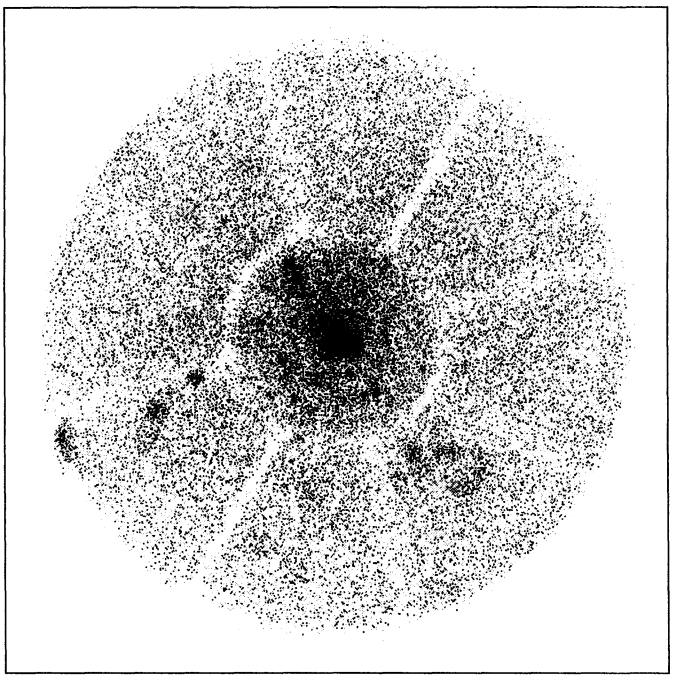

FIG. 1.—Raw PSPC data of NGC 4636. All spectral channels are included. A factor of 30 compression is used for display. North is at top and East to the left.

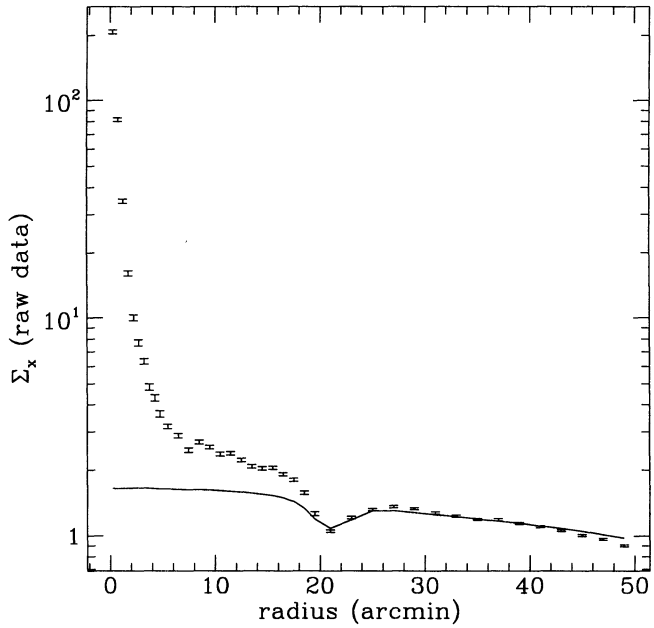

FIG. 2.—Radial profile (in counts/pixels, with pixels of 15′ × 15′) of the total raw detected counts (*points*) and the background template (*solid line*) adopted in this analysis. Individual sources have been masked out and do not contribute to the profile.

To study the morphology and to quantify the significance of the source emission and extent we must first obtain a reliable estimate of the field background in the region covered by the source. A detailed discussion of how we arrived at the background template used in this work is given in Appendix A. Figure 2 shows the raw count radial profile, together with the background model adopted.

To obtain the radial profile, photons in the 0.1–2.0 keV band are binned in concentric annuli of 0.5–1′ width, and averaged over 360° azimuthal angle. The source is clearly extended, with intensity smoothly declining out to ~18′ (outside of 18′ the support structure is partially shadowing the field); moreover, the photon radial distribution flattens significantly at radii greater than $r \sim 6'$–$8'$. The isointensity contour map shown in Figure 3 also confirms the presence of a low surface brightness component that fills an inner $\geq 15'$ circle and is more prominent in the NNW direction. The data plotted in Figure 3, in the 0.1–2.0 keV band, are normalized to the effective exposure, so that the modulation due to vignetting and the obscuration by the window support structure are taken out (we have used the average exposure file provided with the standard on-line analysis), and are smoothed with a Gaussian function, with $\sigma = 30''$. A flat term of 0.0021 count arcmin^{-2} s^{-1} is subtracted, corresponding to the "corrected" count rate in the 25′–27′ region.

To reassure ourselves that the emission outside of 8′ is real source emission and is not a spurious consequence of the uncertainty in the definition of the background, we have also compared its spectral shape with that of a region farther out, where background counts should dominate. Figure 4 shows a direct comparison of the 10′–15′ region (cleaned of the contribution from individual sources) with the 25′–27′ background annulus. For the 25′–27′ annulus, both the observed distribution and that obtained after the vignetting correction appropri-

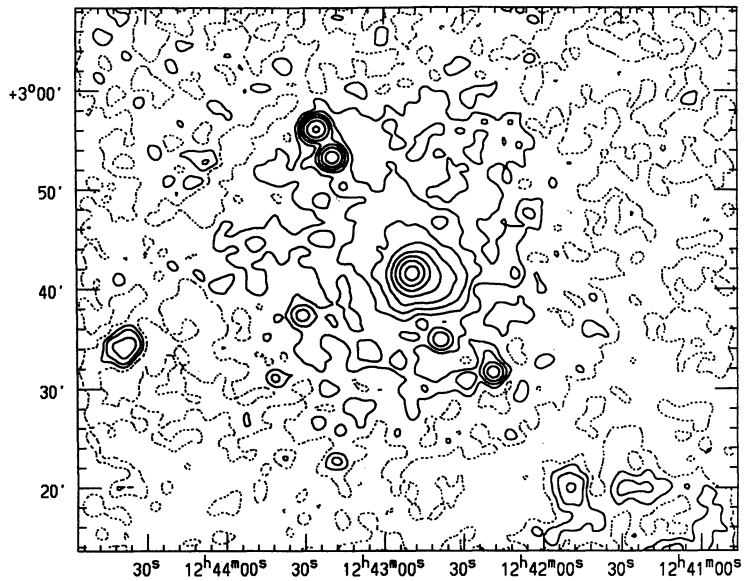

FIG. 3.—Isodensity X-ray contour maps of the central portion of the PSPC field centered on NGC 4636. The data (0.1–2 keV band) have been smoothed with a Gaussian with $\sigma = 30''$, "flat-fielded" using the exposure map and background-subtracted. Contour levels are: 0 (*dashed*), 0.04, 0.08, 0.16, 0.31, 0.62, 1.25, 2.5, 5 counts arcmin^{-2}.

ate for the 10′–15′ region has been applied are shown (the background data are actually offset for clarity). The two distributions are clearly different, their ratio increasing with energy suggesting that the spectrum of the background annulus is softer than that of the 10′–15′ region. It is clear that vignetting could not account for such a significant change in spectral characteristics (see also Appendix A), and therefore the excess emission outside 8′ should be regarded as a real astrophysical feature. Its nature will be discussed further on.

2.2. *Radial Count Distribution*

The azimuthally averaged radial profile of the net galaxy emission, where the background is subtracted and the contribution from the individual sources in the field is masked out, is shown in Figure 5: a change of gradient is clearly observed at $r \sim 6'$–$8'$, with excess emission out to $r \sim 18'$ from the source center. Inspection of Figure 3 in fact shows a more complicated, nonradially symmetric surface brightness distribution. At 2′–6′ radius, a distortion in the X-ray isophotes is visible in the SW quadrant, while at larger radii the northern sector appears more prominent than the southern one. Figure 6 compares the radial distributions for different azimuthal angles.

The radial profiles of normal galaxies, in analogy with clusters of galaxies, have been usually parameterized with a "King" model of the form $\Sigma_X \propto [1 + (r^2/r_X^2)]^{-\alpha}$, where r_X is the core radius. However, the core radii are generally much

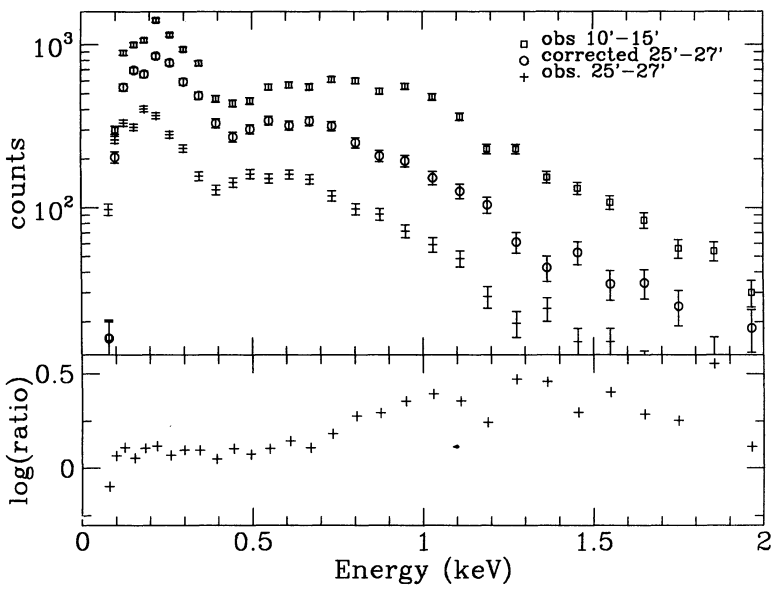

FIG. 4.—Comparison of the spectral shape of the annulus 10′–15′, and of the 25′–27′ background region in NGC 4636. The bright individual sources visible in the contour maps are masked out. The ratio (log) of the source and the (vignetting-corrected) background count are shown in the lower panel.

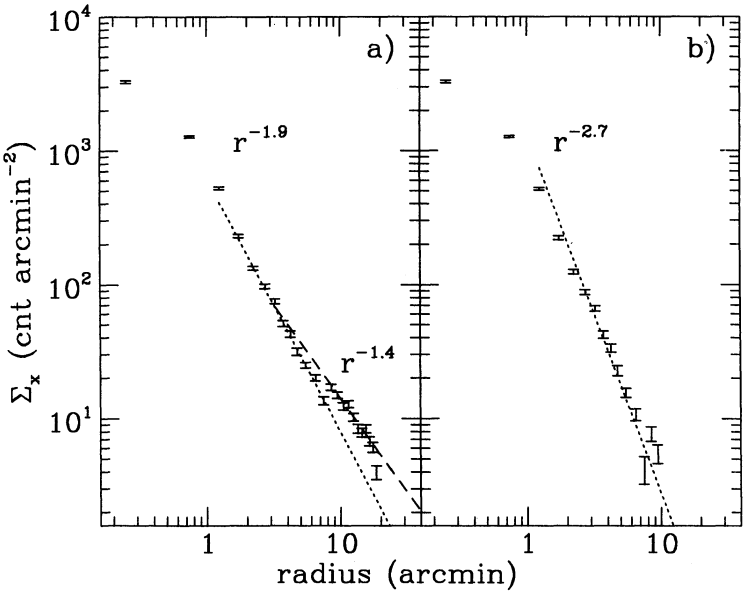

FIG. 5.—Radial surface brightness profile of the net emission from the galaxy, in the 0.1–2.0 keV band. Power-law fits are plotted on the data. (*a*) The background is obtained from the properly normalized exposure map (see text, Fig. 2). (*b*) The background is obtained from the 10′–15′ region.

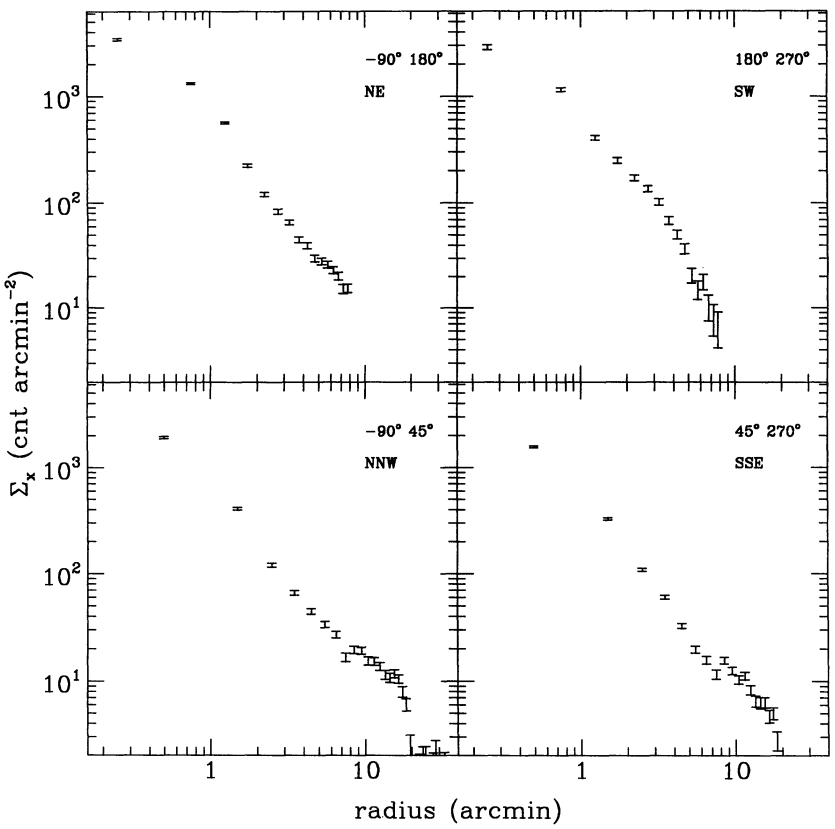

FIG. 6.—Radial surface brightness profile of the net emission from different sectors. The profile is calculated out to $r = 10'$ only in the NE and SW regions (*top panels*), and to $r = 18'$ in the NNW and SSE. The background is obtained from the properly normalized exposure map as in Fig. 5*a*.

smaller than the PSPC point-spread function, and in particular the *Einstein* HRI data indicate $r_X \sim 15''$ for NGC 4636 (TFC). We have therefore fitted the profile only at large radii, where the profile can be approximated with a power-law model. The best-fit slope for the azimuthally averaged profile changes significantly at 6′–8′. We find $\Sigma_X \propto r^{-1.90\pm0.05}$, for $r < 8'$, and $\Sigma_X \propto r^{-1.42\pm0.13}$ for $r > 8'$. If we exclude the SW quadrant in the 2′–6′ region, $\Sigma_X \propto r^{-1.70\pm0.08}$, while the SW quadrant alone is not well fitted by a power law, as clearly shown by Figure 6.

A significantly different profile is also observed outside 8′ in the NNW and SSE directions: $\Sigma_X \propto r^{-1.0\pm0.1}$ in the $-90°$ to 45° angle region (NNW), while $\Sigma_X \propto r^{-1.70\pm0.15}$ in the 45°–270° region (SSE). In the former, the change in slope relative to the inner region is also more pronounced, although the fact that the inner region shows distortion along a different angle might influence in part this evidence.

2.3. *Spectral Data*

The average spectral count distribution of the whole source is extracted from a circle with $r = 18'$. The contribution of the individual sources visible in Figures 1 and 3 is masked out. The background is obtained from the same field, so it has the spectral shape appropriate to this observation. Background counts must then be obtained far from the field center, in a concentric annulus at 25′–27′, to avoid the contribution from the extended source and the support structure of the PSPC. Due to the radial dependence of the intensity and spectrum of the background (see Fig. 2 and Appendix A), both level and spectral shape must be readjusted to the appropriate distance from the field center. The net spectrum shown is therefore the sum of the net counts in concentric annuli, obtained by subtracting an appropriately rescaled background level. The scaling applied to each annulus is obtained from the expected modification at each radius due to the telescope vignetting and instrument response to a flat component with a $kT = 0.3$ keV spectrum, solar abundances, and no absorption (i.e., $N_H = 10^{18}$ cm^{-2}; see Appendix A).

The spectral analysis is based primarily on the PROS software spectral routines, that, in analogy with "SASS" (Standard Analysis Software System), bins the 256 channels of pulse height information in 34 channels, for subsequent use in the spectral fits (see *ROSAT* Data Production Guide, by Downes, White, and Reichert).

We have adopted a thin plasma thermal model with lines (Raymond code in the IRAF "xray" package) and low-energy absorption to fit the observed spectral count distribution. One-hundred percent cosmic abundances (Allen 1973) are assumed as our basic model parameters. The value of N_H is free to vary between 4×10^{19} and 4×10^{20} cm^{-2} (the line-of-sight galactic value is 1.7×10^{20} cm^{-2}; Stark et al. 1992). Different choices of abundance percentages and N_H limits are discussed in the next section. We have included in the fit as many channels as possible, with the following restrictions: (1) the boundary channels should have a signal-to-noise ratio greater than 2; (2) only channels with more than 10 total counts are included, so that the source count errors could be computed as the square root of the counts; (3) channels, 1, 2, and 3 are not used, to avoid "bad" or marginal PI channels at the soft energies (*ROSAT* Data Production Guide); and (4) channels above 30 are not used, to avoid discontinuities in the background rescaling factors (see Appendix A; however, since the counts in these channels are usually very low, we would have excluded them because of restriction 2). The results are summarized in Table 1.

The very large number of counts obtained in this observation allows us to study the spectral characteristics of this source in different regions. We have analyzed the 0′–8′ circle as a whole and in several concentric annuli. We have also divided the outer region in separate annuli.[5]

The results obtained for each annulus indicate a complex spectrum. The two innermost annuli cannot be fitted with a single-temperature model. The χ^2 values are very high, and the structure of the residuals about the best fit indicate a contribution to the high χ^2 value from all channels. Figure 7 shows an example for the residuals in the innermost region ($r = 1'$). The addition of a second component dramatically improves the quality of the fit, and the residuals are now more homogeneously scattered around a value of 0, although the χ^2_{min} value is still relatively high. The F-test applied to the results of the one-temperature and two-temperature fits above confirms that the addition of the additional parameters significantly improves the fit ($P > 0.99\%$). The best-fit χ^2 value is further lowered by the addition of a third thermal component to the model spectrum. Figure 8 shows the final fit to the spectral distribution of counts in the inner 1′ circle. In the 2′–8′ region, a one-temperature fit is adequate, since the χ^2 values are not significantly improved by a second component, as shown by the results summarized in Table 1 (we list the results for a two-temperature fit for all annuli for completeness).

Outside 8′, the two-temperature model again gives significantly improved fits over the single temperature, although there is no clear trend: the lower temperature is ill-defined, while the higher temperature is consistently above $\sim$0.8–1 keV. The average temperature for the whole region is significantly higher than the average temperature in the inner 8′ region, and the low-energy absorption is significantly lower.

We have also looked at the temperature distribution in the SW quadrant, compared to the rest of the azimuthal plane, to see whether the morphological distortion could also be related to a different radial temperature profile. To retain enough statistics in the SW quadrant, we have looked at the 2′–3′ and 3′–6′ annuli, in the two azimuthal angles 180°–270° (SW) and 270°–180° (NE). With a single-temperature model, the temperatures in the SW quadrant in both annuli are lower than in the complementary region at the 68% level for two interesting parameters, although they are consistent at the 90% confidence level.

2.4. *Element Abundance and Low-Energy Absorption*

We have investigated whether cosmic abundances, at 100% value, should be used, or whether a different percentage and/or a different model should be considered. For this purpose, we have set all parameters (N_H, kT_1, kT_2, abundance percentage) free to vary, and compared the results.

We find that with the present data the determination of the abundance percentage is not possible, since the coarse energy

[5] To perform the spatially resolved spectral analysis correctly, one has to be able to take into account the spatial and spectral characteristics of the instrument at the same time. The software currently available does not allow us a proper treatment of these data. With PROS were were able to account for a vignetting-corrected area table appropriate for the extended region covered by the source and for the background region. However, it is unlikely that the hardening of the spectral counts is an instrumental artifact, and we should be justified in "believing" the substance of our results, bearing in mind that the details should be refined at a later time.

TABLE 1

100% COSMIC ABUNDANCE MODEL, WITH LOG N_H FREE TO VARY IN THE RANGE 19.6–20.6

Annulus	Counts	Error	Channel	N_H	90% Error	kT_1	90% Error	Norm[a]	kT_2	χ^2	DOF	Notes
0–1.....	4963.6	71	[4:29]	19.94	19.85–20.05	0.583	0.56–0.67	...	...	95.0	23	a
				20.19		0.459	<0.55	−0.20	1.13	39.2	21	b
				20.60		0.575		−0.10	0.12	19.6	19	c
1–2.....	3182.9	59	[4:29]	19.87	19.75–19.95	0.724	0.69–0.76	...	...	47.2	23	a
				20.07		0.641	<0.68	−0.02	2.71	18.2	21	b
2–3.....	1732.6	47	[4:28]	19.84	19.70–20.05	0.795	0.75–0.84	...	...	21.1	22	a
				19.93		0.764		−0.42	2.89	19.1	20	d
3–4.....	1329.7	44	[4:28]	19.97	19.75–20.15	0.859	0.81–0.92	...	...	14.9	22	a
				20.01		0.845		−0.71	2.89	14.5	20	d
4–6.....	1813.2	61	[5:27]	19.69	<20.00	0.896	0.84–0.94	...	...	22.2	20	a
				19.70		0.868		−0.08	0.93	22.2	18	d
6–8.....	1342.5	66	[4:26]	19.60	<19.75	0.878	0.78–0.95	...	...	22.4	20	a
				19.60		0.726		0.26	3.00	13.9	18	d
8–10.....	1781.0	79	[4:29]	19.60	<19.7	0.939	0.87–1.05	...	...	58.3	23	a
				19.75		0.226	0.10–0.45	0.44	1.48	16.8	21	b
10–12.....	2152.9	99	[5:27]	19.60	<19.7	1.028	0.93–1.13	...	...	49.9	20	a
				20.00		0.190	0.10–0.40	0.34	1.02	17.0	18	b
12–15.....	1691.7	103	[4:27]	19.60	<19.8	1.002	0.86–1.13	...	...	44.4	21	a
				19.60		0.529	>0.20	0.74	3.00	26.0	20	b
15–18.....	1974.3	131	[5:26]	19.60	<19.85	1.078	0.96–≥ 1.2	...	...	30.9	19	a
				19.60		0.811		0.69	3.00	24.2	17	b
0–8.....	14466	145	[4:30]	19.76	19.70–19.85	0.745	0.73–0.76	...	...	142	24	a
				19.95		0.669		−0.03	2.74	47.8	22	b
8–18.....	7725	312	[4:29]	19.60	<19.70	1.021	0.95–1.09	...	...	65	23	a
				19.60		0.579		0.73	2.25	32.3	21	b
0–18.....	22249	293	[4:30]	19.60	<19.70	0.816	0.79–0.83	...	...	197	24	a
				19.71		0.674		0.20	2.75	67.3	22	b

[a] Log of the ratio of the second component normalization relative to the first component [i.e., log (N2/N1)].

NOTES.—(a) One-temperature fit. The 90% errors quoted are for (2) interesting parameters ($\chi_{min} + 4.6$). (b) Two-temperature fit. No errors are quoted for N_H, kT_2 (see appendix B). (c) Three-temperature fit, with $kT_3 = 3$ keV. (d) Best-fit parameters for a two-temperature fit included only for completeness. No errors are calculated.

resolution of the PSPC allows for several equivalently acceptable formal solutions that have significantly different meanings. Details can be found in Appendix B. A graphical explanation of this is shown in Figure 9, where we show three significant examples applied to the 0′–1′ spectral data: (1) a 100% cosmic abundance model, with N_H at the Galactic value along the line of sight and three temperatures free to vary; (2) a 100% cosmic abundance model, with N_H and two temperatures all free to vary; (3) a low-abundance, that is, 20%, cosmic model, with N_H and one temperature free to vary. However, these are not exhaustive of all possible ambiguities in the spectral fit of these data (see also Appendix B).

Two feature are immediately clear from Figure 9: (1) in the 100% cosmic abundance model, a stronger soft component can compensate for a higher column density (Figs. 9*a* and 9*b*); (2) a single temperature with low cosmic abundance (20%) and absorption consistent (to within the 90% confidence) with the Galactic line-of-sight column density gives an equally acceptable fit to the data. In all three cases in the figure the residuals are relatively well behaved, and although formally the fit in

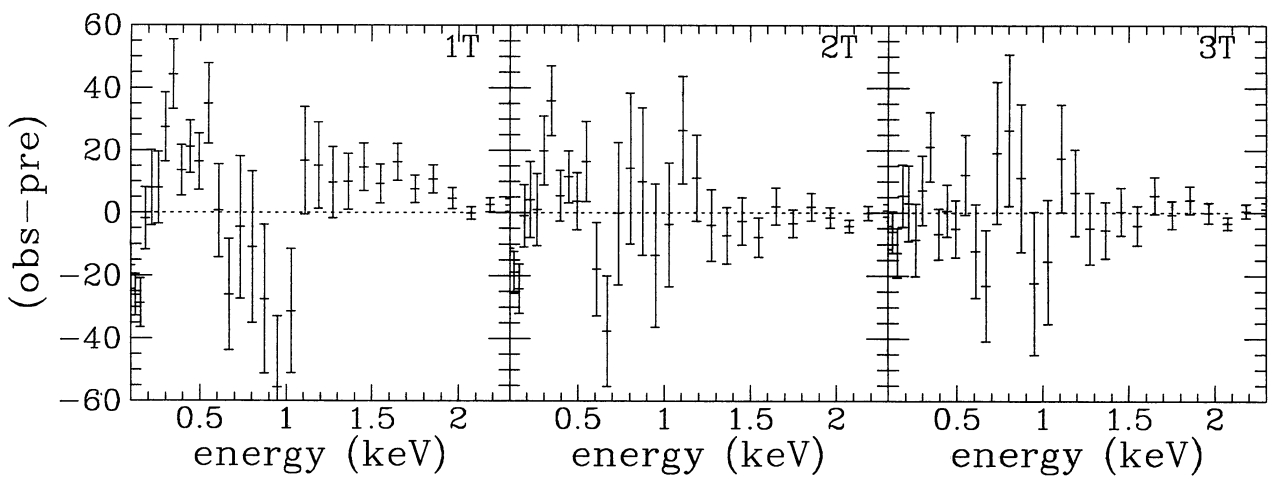

FIG. 7.—Residuals (observed-predicted) from the one-temperature, two-temperature, and three-temperature, 100% cosmic abundance models in the 0′–1′ region (from the fits in Table 1).

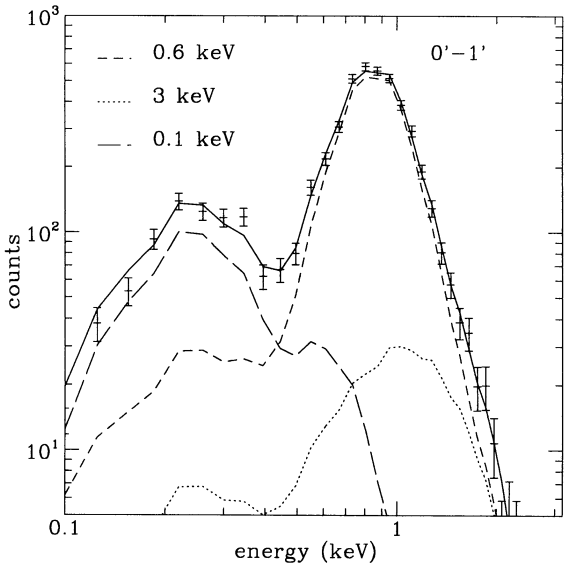

FIG. 8.—Best-fit three-temperature model in the inner 1′ region (from Table 1).

Figure 9*b* gives a higher value of χ^2, we believe that this is not sufficient to consider it significantly poorer than the others (see Appendix B, Fig. 7).

The temperature and N_H variations at different radii for a one-component model at 20% cosmic abundance (the lowest value investigated here) are summarized in Table 2, which indicate clearly that the temperatures increase out to 4′–6′ from $kT \sim 0.5$ to $kT \sim 0.8$ keV, and then remain constant at 0.8–1 keV.

We therefore conclude that our results on abundance are heavily dependent on what assumption we keep: if one temperature only is allowed, then low-abundance models ($\lesssim 40\%$) only can fit the data in the inner 2′. If, however, multitemperature gas is allowed, then cosmic abundances are possible; however, trade-offs between high absorption and a very soft component are required. For Galactic line-of-sight column densities, three temperatures are required in the inner 1′. However, regardless of which model is assumed, the temperature (or the dominant component, in a multitemperature fit) is fairly insensitive of the abundance percentage/low-energy absorption chosen.

We also notice that the values of the column density drop significantly outside of 6′–8′ relative to the inner regions. This result is independent of the metal abundance (see Tables 1 and

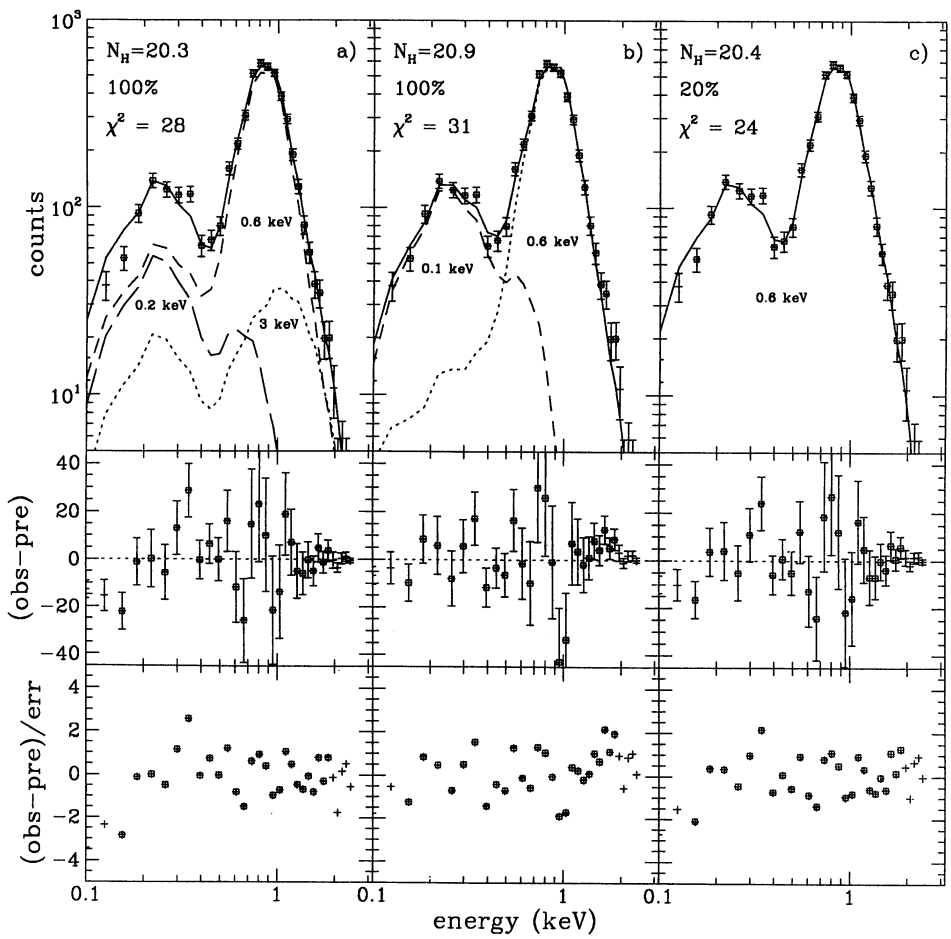

FIG. 9.—Comparison of the various best-fit models in the inner 1′ region. The data and models are shown in the top panels for (*left*) 100% cosmic, line-of-sight N_H, 3 T model; (*center*) 100% cosmic, free N_H and 2 T model; (*right*) 20% cosmic, 1 T model. Middle and bottom panels show the corresponding residuals: (observed-predicted) and (observed-predicted)/error.

TABLE 2

20% COSMIC ABUNDANCE MODEL

Annulus	Counts	Error	Channel	N_H	90% Region	kT	90% Region	χ^2
0–1	4963.6	71	[4:29]	20.44	20.40–20.50	0.575	0.55–0.61	23.8
1–2	3182.9	59	[4:29]	20.43	20.40–20.50	0.687	0.65–0.72	15.9
2–3	1732.6	47	[4:28]	20.43	20.35–20.50	0.751	0.70–0.79	39.4
3–4	1329.7	44	[4:28]	20.46	20.35–20.55	0.804	0.75–0.86	27.7
4–6	1813.2	61	[5:27]	20.35	20.20–20.40	0.844	0.79–0.89	32.7
6–8	1342.5	66	[4:26]	20.04	19.85–20.20	0.781	0.70–0.87	8.8
8–10.....	1781.0	79	[4:29]	19.90	19.80–20.10	0.825	0.75–0.95	19.9
10–12.....	2152.9	99	[5:27]	19.87	19.60–20.00	0.888	0.78–0.98	16.8
12–15.....	1691.7	103	[4:27]	19.96	19.65–20.20	0.875	0.75–1.02	28.4
15–18.....	1974.3	131	[5:26]	19.87	<20.20	0.956	0.84–1.15	19.8
0–8	14466	145	[4:30]	20.37	20.35–20.45	0.705	0.69–0.71	34.4
8–18.....	7725	311	[4:29]	19.96	19.80–20.10	0.905	0.83–0.97	27.6
0–18.....	22249	293	[4:30]	20.21	20.15–20.25	0.755	0.73–0.77	55.1

2) although the value of N_H depends on the model assumed, as discussed above.

2.5. *Background*

As will be discussed later, there is a distinct possibility that the emission outside 8′ is not directly related to the galaxy, and should therefore be subtracted from the inner region. We have therefore produced an azimuthally averaged profile of the inner 8′ region, using the outer 10′–15′ annulus as background (cf. § 2.2). The resulting surface brightness distribution is shown in Figure 5*b*. A power-law fit to the 2′–8′ radial range gives $\Sigma_X \propto r^{2.68\pm0.18}$.

We have also repeated the spectral analysis of § 2.3 in the inner 8′ region, using the properly rescaled (and vignetting-corrected as described in Appendix A) count distribution obtained in the 10′–15′ region as background. For statistical purposes we have treated the 4′–8′ annulus as a single region. Table 3 summarizes the results for the 100% and 20% cosmic abundance models. As in § 2.4, only one temperature is required for low abundances, while two temperatures are still needed in the inner 2′ for 100% cosmic, and the best-fit values are entirely consistent with those of Tables 1 and 2.

2.6. *Fluxes and Luminosities*

We have calculated the flux and luminosity of the source under the various assumptions used above. The results are summarized in Table 4 and are the sum of the flux (luminosity) for each annulus for the best-fit value obtained under the assumed model (Tables 1, 2, 3). The luminosity of the whole source is of 6–7 $\times$ 10^{41} ergs s^{-1}, for 20%–100% cosmic abundance.

For completeness, we also give in Table 5 the net counts and the fluxes of the five sources visible within $r \sim 18'$, that have been subtracted. The fluxes are calculated assuming the line-of-sight column density and a power-law spectrum $f(E) = AE^{-\alpha_E}$, with $\alpha_E = 1.7$, which is very close to the best-fit spectrum for two of the three strong sources. Four source 4 we have used $\alpha_E = 0.9$, the best-fit value.

3. SUMMARY OF RESULTS

The results from the previous sections can be summarized as follows:

Both maps and surface brightness profiles indicate that there is emission at least out to $r \geq 18'$. Investigation of the possi-

TABLE 3

SPECTRAL RESULTS FOR SOURCE COUNTS ABOVE A LOCAL (10′–15′) BACKGROUND

A. 100% COSMIC ABUNDANCE MODEL

Annulus	Channel	N_H	kT	Norm[a]	kT_2	χ^2
0′–1′.....	[4:29]	19.95 (19.85–20.05)	0.582 (0.55–0.62)	...	...	91.8
		20.16	0.507	−0.1658	1.9	39.8
1′–2′.....	[4:29]	19.91 (19.80–20.00)	0.719 (0.68–0.75)	...	...	41.0
		20.09	0.642	−0.0389	2.8	16.9
2′–3′.....	[4:28]	19.96 (19.80–20.15)	0.786 (0.74–0.83)	...	...	22.7
		19.99	0.768	−0.8056	1.8	22.3
3′–4′.....	[4:28]	20.19 (20.00–20.40)	0.854 (0.80–0.93)	...	...	15.3
		20.19	0.856	0.0729	0.8	15.3
4′–8′.....	[5:25]	20.06 (<20.60)	0.861 (0.78–0.92)	...	...	19.1
		20.05	0.861	−0.0354	0.8	19.1

B. 20% COSMIC ABUNDANCE MODEL

Annulus	Channel	N_H	(90% Range)	kT	(90% Range)	χ^2
0′–1′.....	[4:29]	20.44	(20.40–20.50)	0.574	(0.55–0.60)	23.5
1′–2′.....	[4:29]	20.45	(20.40–20.50)	0.684	(0.65–0.72)	15.3
2′–3′.....	[4:28]	20.49	(20.40–20.60)	0.742	(0.69–0.79)	43.1
3′–4′.....	[4:28]	20.59	(20.50–20.80)	0.789	(0.74–0.86)	29.9
4′–8′.....	[5:25]	20.52	(20.30–21.00)	0.810	(0.73–0.90)	28.7

[a] Log of the ratio of the second component normalization relative to the first component.

TABLE 4

FLUXES AND LUMINOSITIES OF THE SOURCE ASSOCIATED WITH NGC 4636

Radius	f_X (ergs cm^{-2} s^{-1})	L_X (ergs s^{-1})	Model[a] (cosmic)	
0′–8′	10.47×10^{-12}	3.65×10^{41}	100	
0′–18′.....	16.97×10^{-12}	5.92×10^{41}	100	
0′–8′	14.50×10^{-12}	5.06×10^{41}	20	
0′–18′.....	21.15×10^{-12}	7.38×10^{41}	20	
0′–8′	9.38×10^{-12}	3.27×10^{41}	100	local background
0′–8′	9.54×10^{-12}	3.32×10^{41}	20	local background

[a] Either 100% or 20% cosmic abundance spectral models are used to convert from counts to X-ray fluxes. "Local background" is obtained from the 10′–15′ annulus around the galaxy (see text).

TABLE 5

FLUXES FOR THE POINT SOURCES EMBEDDED IN THE NGC 4636 EMISSION

Source	R.A. (J2000)	Decl. (J2000)	Counts	Error	Flux (ergs cm^{-2} s^{-1})
1.....	12:42:19.3	2:31:32.8	208	20	4.6×10^{-13}
2.....	12:42:38.7	2:34:46.6	125	19	2.3×10^{-13}
3.....	12:43:19.8	2:53:04.9	995	35	2.1×10^{-12}
4.....	12:43:25.6	2:55:53.8	733	31	1.3×10^{-12}
5.....	12:43:31.0	2:37:17.2	107	17	2.0×10^{-13}

NOTE.—The flux is in the 0.1–2 keV band and is obtained assuming a power-law spectrum with Galactic absorption and $\alpha_E = 1.7$. For source 4, $\alpha_E = 0.9$.

bility that emission could be detected farther out is beyond the scope of this paper.

A significant discontinuity in an otherwise smooth radial profile is observed at $r \sim 8'$: $\Sigma_X \propto r^{-1.90 \pm 0.05}$, for $r < 8'$; $\Sigma_X \propto r^{-1.40 \pm 0.13}$ outside. However, azimuthal asymmetries are found in the 2′–6′ region, more prominent to the SW, and the emission in the NNW sector appears stronger than in the SSE one outside of 8′.

With the present data we cannot discriminate between different abundance models, unless we assume that the gas is homogeneous, with a single temperature at any given radius. However, the values of the best-fit temperatures do not change significantly with abundance percentages.

Similarly, we cannot determine accurately the N_H value, which is highly model dependent. In general, low-abundance models require higher N_H values; alternatively a very soft component can be added to compensate for high absorbing columns.

The average temperature and column density are significantly different in the regions within and outside of 8′: lower values of N_H and higher temperatures are measured in the 8′–18′ region, regardless of the abundance assumed.

Specifically for the region within $r = 8'$, for galactic absorption:

The spectral characteristics of the emission indicate that two/three temperatures are needed to explain the observations, for all but very low abundance models. The high-temperature component is easily distinguished from the low temperature only out to a radius $r \sim 2'$, and cannot be constrained to better than $kT_2 > 0.9$ keV. Its contribution is significant and can be comparable to that of the softer component. These can be the result of the two physical situations: the gas spans a range of temperatures, and only two (three) are selected, one of which best matches the instrument spectral response; (2) there are two components, a hotter one (possibly isothermal) at $kT > 0.9$ keV, and cooler gas probably more centrally peaked (possibly a cooling flow), coexisting with the hotter phase, with temperatures increasing outward.

In the assumption of very low abundances, one temperature at any given radius can explain all the data. In this case there is a clear temperature gradient, from $kT \sim 0.5$ to ~ 0.9 keV.

Outside $r = 8'$:

There is a similar trend as in the inner region, with high-abundance models requiring more than one temperature. For 20% abundance, the temperature is roughly constant at $kT \sim 0.9 \pm 0.2$ keV.

The column density has significantly lower values than in the inner region, and could be significantly lower than the Galactic column density along the line of sight to NGC 4636. However, as discussed above, this evidence should be taken with caution.

4. COMPARISON WITH PREVIOUS RESULTS

X-ray images of this galaxy obtained with the *Einstein* Observatory IPC and HRI (TFC; Forman et al. 1985) have revealed a relatively symmetric source, extended out to $r \sim 6'$. Outside of this radius, excess emission was detected, in the 7′–10′ region, which, however, could not be unambiguously attributed to a real astrophysical feature, rather than an instrumental artifact.

A comparison of the radial distribution from the *Einstein* instruments and the *ROSAT* PSPC indicates that the excess emission outside 6′ is indeed a real astrophysical feature, which extends from ~8′ to 18′. Inside 6′ the profiles are comparable, once the different instrumental responses are taken into account.

The spectral characteristics of the emission of NGC 4636 were investigated both with the IPC and with the LAC on board the *Ginga* satellite (TFC; Kim, Fabbiano, & Trichieri 1992; Awaki et al. 1991). A thin thermal model, with temperature in the range 0.7–1.1 keV, was fitted to the whole source, but neither instrument would allow a significant study of spatially resolved spectra.

The average temperature obtained from the PSPC data, for the whole source (both out to 8′ and to 18′) and under the assumption of a one-component temperature is consistent within the 90% confidence region with previous results, although it indicates an average temperature significantly softer than 1 keV.

5. INTRINSIC PROPERTIES

The quantities derived above, namely radial surface brightness profile and temperatures, are obtained from the observed counts at each projected radius, which are contaminated by the outer layers projected along the line of sight. To obtain the intrinsic count distribution we have used the technique described by Kriss, Cioffi, & Canizares (1983) to deproject the radial surface brightness profile and subtract the contribution of the external layers. Once the temperature is known at any given radius, the gas density and cooling time can be easily derived from the observed radial profile.

However, if the gas has a temperature gradient, or is inhomogeneous at all radii, as suggested by the results above, then the quantities derived suffer from the same contamination as

the count distribution. In particular, we expect that the intrinsic temperature gradient should be steeper than that derived from the data. Moreover, it is important to check that the requirement of a multitemperature fit (for the 100% cosmic abundances) is not induced by the superposition of the outer hotter layers onto the central cooler component.

As already discussed, to properly take this into account, a detailed combination of the two-dimensional spatial and spectral characteristics of the instrument with the assumed spectral fit should be used. Here we have applied the same deprojection technique to each single spectral channel, so that the subtraction of the contribution from the adjacent outer layer takes into account both intensity and spectral shape. Since it is likely that the emission outside of 8′ is not related to the galaxy and should be regarded as "background" for this purpose (see § 7), we have started our deprojection from an outer radius of 8′ (see Fig. 5*b*). We have also disregarded azimuthal asymmetries and treated the source as spherically symmetric.

Table 6 summarizes the results for 100% and 20% cosmic abundances. We find that the main results of the previous section are confirmed. Acceptable fits are obtained for either 20% or 100% models. A multitemperature fit is required for the inner region, for 100% abundances. For $r > 2'$, one component is acceptable. A single component only is required for 20% abundances at all radii For the 20% abundance model, the temperature increases from ~ 0.5 to ~ 0.8 out to 3′–4′.

We have then used the temperatures derived in the assumption of low cosmic abundances to obtain a density profile, shown in Figure 10. For 20% abundance, we could use the spectral fit results directly. To use the 100% cosmic model, we would have to know how to decompose the emission in the various components. However, since the higher temperature is not well defined, and the evidence of a finite number of components probably indicates that the gas is inhomogeneous, we have restricted ourselves to the simpler scenario of homogeneous gas with a temperature gradient.

For completeness, we have also "deprojected" the surface brightness profiles out to the last observed point (18′), both in the assumption of azimuthal symmetry and separately for the northern and southern regions outside of 8′. The radial density

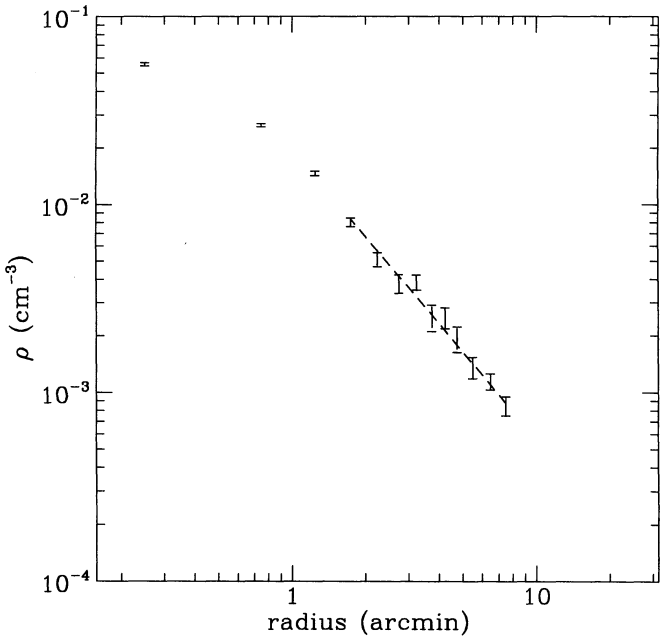

FIG. 10.—Density distribution (ρ) for 20% cosmic abundance models. Deprojection starts at the 6′–8′ annulus. A power law $r^{-1.55}$ is plotted on the data.

profiles obtained assuming a constant temperature at 0.9 keV are shown in Figure 11. In the 0′–8′ region the data are azimuthally averaged over 360° in all three plots and are directly comparable to Figure 10. The differences in the common region, due to the different background subtraction and the choice of temperatures, are not significant (probably well within the uncertainties in the other assumptions, like spherical symmetry, distances). A significant flattening of the profile is observed however at radii larger than 6′–8′ in all the plots.

6. GAS PROPERTIES

The average gas temperature, both observed and "intrinsic" (Tables 1, 2, 6), shows a positive gradient with radius out to $r \sim 6'$, although we cannot clearly establish whether a single or

TABLE 6

RESULTS FROM THE DEPROJECTED SPECTRAL DISTRIBUTION

A. 100% COSMIC ABUNDANCE MODEL

Annulus	N_H	90% Region	kT	90% Region	Norm[a]	kT_2	90% Region	χ^2
0′–1′.....	20.00	[19.80–20.10]	0.55	[0.50–0.60]	...	...	...	56
	20.20		0.49	[<0.55]	−0.21	2.2	[>0.7]	31
1′–2′.....	19.90	[19.80–20.05]	0.67	[0.62–0.75]	...	...	...	29
	20.26		0.35	[<0.6]	0.14	0.90	[>0.6]	12
2′–3′.....	19.70	[<20.20]	0.72	[0.60–0.82]	...	...	...	15
3′–4′.....	20.20	[19.80–20.60]	0.86	[0.77–1.00]	...	...	...	15
4′–8′.....	20.06	[<20.60]	0.86	[0.78–0.92]	...	...	...	19

B. 20% COSMIC ABUNDANCE MODEL

Annulus	N_H	90% Region	kT	90% Region	χ^2
0′–1′.....	20.50	[20.45–20.55]	0.55	[0.51–0.58]	22
1′–2′.....	20.45	[20.40–20.50]	0.65	[0.60–0.70]	11
2′–3′.....	20.40	[20.20–20.60]	0.69	[0.58–0.80]	19
3′–4′.....	20.60	[>20.40]	0.80	[0.72–0.87]	21
4′–8′.....	20.52	[20.30–21.00]	0.81	[0.73–0.90]	29

[a] Log of the ratio of the second component normalization relative to the first component.

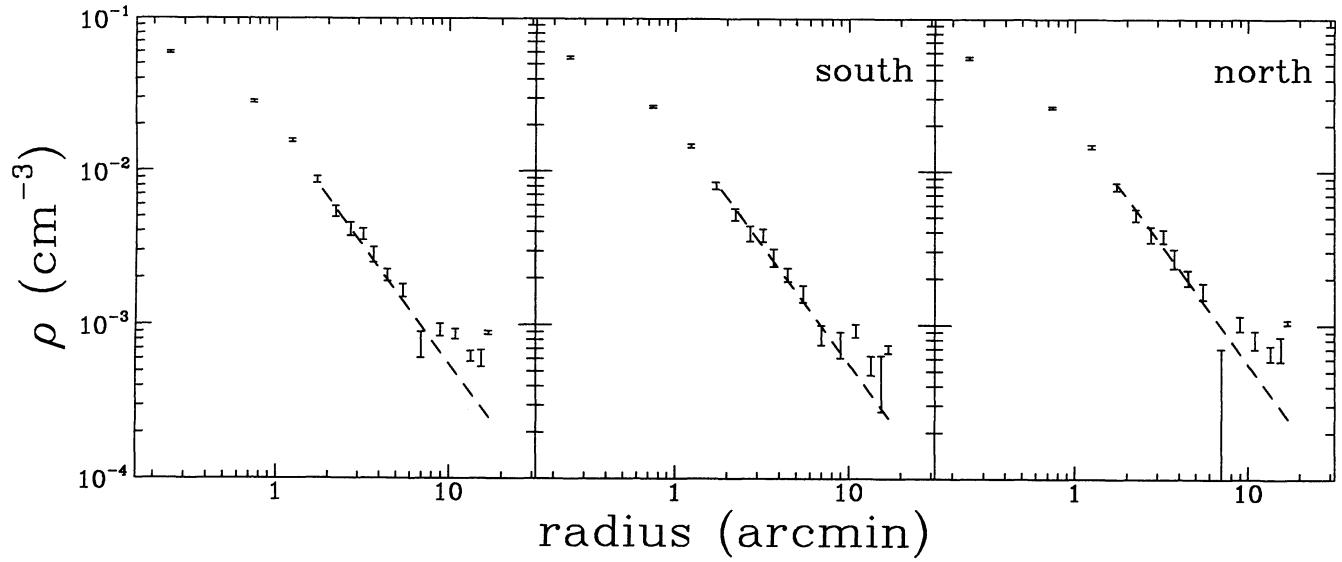

FIG. 11.—Density distribution (ρ) for 20% cosmic abundance models and a constant temperature $kT = 0.9$ keV. Deprojection starts at the 15′–18′ annulus. The same power law $r^{-1.55}$ as in Fig. 10 is plotted on the data.

a multitemperature interstellar medium is present at each radius, nor can we determine the metal abundance. For low-abundance, one-temperature models (Table 6), the azimuthally averaged "intrinsic" temperature of the gas increases with radius as $T \propto r^{\sim 0.2}$, over a scale of $\sim$30 kpc. A comparison with temperature profile models of Vedder et al. (1988) and Bertin et al. (1993) shows that increasing temperature profiles are produced in the presence of external pressure. Heavy halo models, capable of reproducing the observed mean temperature and X-ray luminosity of this object (cf. model D1 in Vedder et al.) would predict at best isothermal gas over most of the galaxy (1–40 kpc).

The minimum external pressure necessary to explain raising temperatures corresponds to environments like those in loose groups or poor clusters (e.g., Pegasus I). Such should not be in the ambient medium of NGC 4636 if this is an isolated object. However, emission outside the optical galaxy is detected, indicating a possible confining medium for the inner gas. Motion against this medium (possibly observed in the asymmetric emission at $r \sim 2'$–$6'$) could also produce significant pressure. Specific models for temperature profiles in the presence of dynamical pressure (stripping) are discussed by Gaetz (1985). For a model that allows for little gas loss ("nearly complete gas retention"), which would be appropriate for this galaxy, temperatures averaged over spherical shells centered on the galaxy show a significant increase (up to a factor of 10) on scales of 10–20 kpc. A steeper temperature gradient might also be expected on the side of the shock front, which might be suggested by the data.

The total quantity of gas present in NGC 4636 can be determined from the spectral results in the low-abundance model, since it is not possible with the present data to obtain a good measure of the various components, if the abundance is 100% the cosmic value. Inside 8′ $M_{\rm gas} \sim 1$–$2 \times 10^{10}\ M_\odot$, depending on which background is used (the field value from 25′–27′, or a local background from 10′–15′, see § 2.2, 2.5). This constitutes $\sim$2%–6% of the mass in stars (for an optical [blue] mass-to-light ratio of 10). If we extend the estimate to the whole source (18′, see Fig. 11), $M_{\rm gas} \sim 8 \times 10^{10}\ M_\odot$.

Figure 12 shows the comparison of the observed X-ray surface brightness distribution with the optical light (N. Caon et al. 1993, private communication). The X-ray data are azimuthally averaged, while the *B*-band data are along the apparent major axis of the galaxy. However, since the ellipticity is very small for this object (Caon et al.; RC3), these two profiles are directly comparable. The comparison in Figure 12*a* shows that the Σ_X and Σ_o are in good agreement out to $\sim 5'$, as already noticed in the *Einstein* data (TFC), while outside $r \sim 8'$ the optical profile falls off much more rapidly than the X-ray one. A closer agreement between X-ray and optical profiles is observed in Figure 12*b* out to $r = 8'$. Inside 0.5 no direct comparison can be made, since Σ_X is dominated by the PSF of the PSPC.

7. HAVE WE DETECTED EMISSION FROM THE VIRGO CLUSTER AT GREATER THAN 3 Mpc FROM M87?

To understand the properties of the gas inside 8′ it is important to establish the nature of the emission at $r > 8'$, in particular to decide whether it should be subtracted, or whether it should be included in the galaxy's emission as an extension outside the stellar component.

We have considered possible interpretations. We do not believe that the emission at $r > 8'$ has its origin in our Galaxy. NGC 4636 is at high Galactic latitude ($+65°$), and the extent of this emission, if it is a cloud in our own Galaxy, would be less than 100 pc (depending on exactly how far this is), if the emission extends out to the round support structure (see § 2). The observation of a significant drop in the fitted low-energy absorption, and the possibility that the column density $N_{\rm H}$ could in fact be lower than the integrated galactic value along the line of sight (however, see cautionary remarks in § 3), might support a local origin; however, this would be the first detection of $a \sim 1$ keV cloud in the Galaxy. While this certainly does not rule out such a hypothesis, other explanations are more likely.

Likewise, a background source is unlikely. Zwicky et al. (1961–1968) have identified a medium-compact, medium-distance background cluster around this galaxy. At a minimum estimated distance for medium-distance clusters of 15,000 km s^{-1} ($D = 300$ Mpc for $H_o = 50$ km s^{-1} Mpc^{-1}), this source

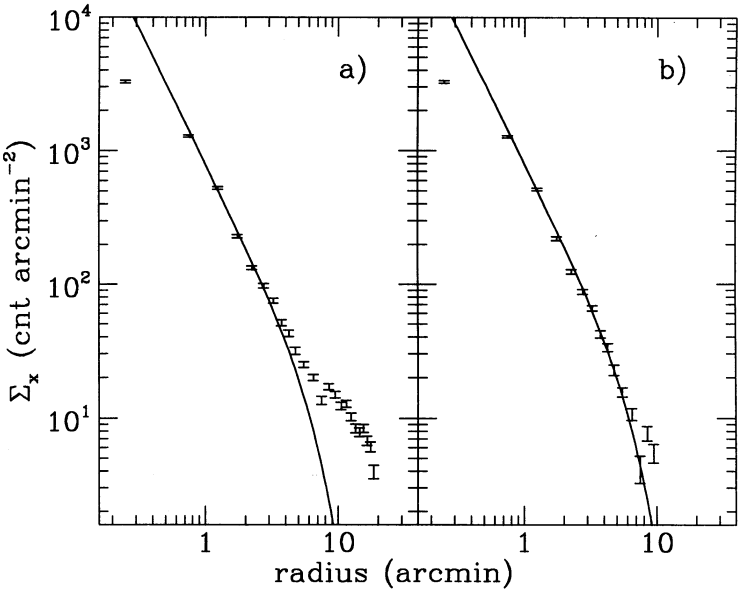

FIG. 12.—Comparison between the optical and X-ray radial distribution. Optical data (arbitrary units) are from Caon et al. (1993, private communication). Since no correction for the very different instrument responses is applied, the discrepancy in the innermost region should not be considered. (*a*) Background from the exposure map as in Fig. 5*a*. (*b*) Background from the 10′–15′ region as in Fig. 5*b*.

would have a linear diameter of more than 3 Mpc and $L_X \gtrsim 10^{44}$ ergs s^{-1}, comparable to the luminosity of rich clusters of galaxies, but with a low temperature around 1 keV.

If this emission is at the distance of NGC 4636, its presence would imply that the gravitational potential in which the galaxy sits is much broader and deeper than the light distribution would suggest. The X-ray source would have a linear diameter greater than 200 kpc, a total X-ray luminosity $L_X \sim 7 \times 10^{41}$ ergs s^{-1}, and a L_X/L_b ratio of 2×10^{31} ergs s^{-1} $L_\odot^{-1}$.

From the results of the deprojection of the azimuthally averaged X-ray surface brightness we found that the density distribution outside $r > 6'$–8′ is significantly flatter than inside and could be consistent with a constant, although it is very ill defind (see Fig. 11). This, coupled with the constant temperature in the 8′–18′ region, would prevent us from any measurement of total mass based on the assumption of gas in hydrostatic equilibrium tracing the gravitational potential (see § 8; Fabricant & Gorenstein 1983), that has ben used in the past and indeed was one of the driving reasons for this observation. For flat density and temperature profiles, $M(r) = 0$ for $r > 8'$ (cf. § 8), while values of a few times 10^{12} $M_\odot$ are found closer in (see below). However, the limited spatial range over which we have measured these quantities, and the relatively large measurement errors due to the poorer statistics at large radii, could explain the lack of detection of a density gradient (isothermal temperatures are actually acceptable), unless we were to discover confinement by some external pressure that would also explain the null mass (since gravity no longer confines the hot gas). This should, however, be coupled with a temperature rise, not required by the present data (although it could be consistent within the errors).

While the discovery of a significant concentration of matter around the poor group NGC 2300 (Mulchaey et al. 1993) could suggest a similar case here, with X-rays tracing the dark matter much more efficiently than the luminous mass (NGC 4636 has always been considered a rather "isolated" galaxy, although at the outskirts of the Virgo cluster), the limits to a density gradient suggest that we are still only detecting the "tip of the iceberg," and therefore that the source is probably uncomfortably large. Moreover, we could not easily explain the stronger emission detected in the northern region outside 8′.

However, as mentioned earlier, we should not neglect the fact that NGC 4636 is at the outskirts of the Virgo cluster. We have therefore considered whether we have detected the cluster gas that extends this far from M87. For a distance of ~20 Mpc for Virgo this would be at a distance of ≥3 Mpc from the cluster center, within the observed extent of other X-ray clusters. In fact the Virgo gas has been traced out ~6° with *ROSAT* survey data (2 Mpc). The observed asymmetry in the inner 6′ would support the idea of interaction with an external medium, not at rest with the galaxy. In fact the distortion in the galaxy's gas could be viewed as a much fainter example of the M86 tail, believed to be the result of that galaxy's motion against the Virgo gas (Forman et al. 1979), and similar possibly to NGC 4472 (TFC).

We have estimated what surface brightness we could expect under the assumption that the radial gradient continues without changes in slope from the cluster center. Extrapolating from the results that Fabricant & Gorenstein (1983) obtained within ~1°.5 from M87 we expect $\Sigma_X \sim 6 \times 10^{-16}$ ergs cm^{-2} s^{-1} arcmin^{-2}. We have detected $\Sigma_X \sim 9 \times 10^{-15}$ ergs cm^{-2} s^{-1} arcmin^{-2}, assuming a flux to count conversion factor appropriate for the same spectral shape and energy band for consistency. We have however measured a temperature close to 1 keV, significantly lower than the temperature of the Virgo cluster gas measured near M87 (Fabricant & Gorenstein 1983), so if this is the same component, the temperature must decline with distance from M87. For $kT = 1$ keV, $\Sigma_X \sim 6 \times 10^{-15}$ ergs cm^{-2} s^{-1} arcmin^{-2}. Clearly a thorough comparison with data at intermediate radii is needed to establish whether the apparent excess that we measure is due to a flattening of the surface brightness profile, suggesting that the simple extrapolation of what is observed close to M87 is not valid at such

large distances, or it is real and due to a different source than the Virgo gas.

8. MASS DETERMINATION

One of the main motivations for obtaining good quality data for this and similar bright early-type galaxies was their potential in providing us with the necessary tools to determine total (gravitational) mass. This can be done by applying the hypothesis of ideal gas in hydrostatic equilibrium in the galaxy's potential (Fabricant & Gorenstein 1983):

$$M(r) = -\frac{kT}{G\,\mu m_{\rm H}}\left(\frac{d\log\rho}{d\log r}+\frac{d\log T}{d\log r}\right)r\,,$$

where k and G are the Boltzmann and the gravitational contants, repectively, $\mu = 0.6$ is the molecular weight, $m_{\rm H}$ is the hydrogen mass, and T is the actual value of the temperature at the radius r.

An attempt to measure masses has already been made with the *Einstein* data; however, the results were uncertain by a large factor ($\gg 10$) mainly due to the uncertainties in $T(r)$ (see TFC). Furthermore, $r_{\rm max} = 6'$ was assumed, but with the possibility that it might be larger. In fact, emission out to at least 10′ was detected, but both the suggestion of a change of slope in the density gradient outside of that radius and a possible instrumental artifact that could simulate emission at $r \sim 8'$–$10'$ made unequivocal determination of $r_{\rm max}$ problematic.

With the *ROSAT* data we were aiming at measuring accurately all four quantities (r, T, $d\log T/d\log r$, $d\log\rho/d\log r$), hence at obtaining an accurate mass measurement at all radii. However, since the spectral fit results are rather complicated, and cannot conclusively point to a one preferred model, we cannot unambiguously resolve this question. Moreover, if there is external pressure, as would be inferred from the rising temperatures and from the detection of emission at radii greater than 8′, the assumptions used in the formula above are no longer valid.

We have nonetheless investigated the case of 20% cosmic abundance, for which we have obtained a temperature measurement at each radius. The outer radial bin for mass measurements is 6′–8′, or $\langle r\rangle = 7'$ (35 kpc for $D = 17$ Mpc). For larger radii either the emission belongs to a separate component or we must await better data to measure temperature and density gradients. The profile of mass versus radius is shown in Figure 13. We have used the overall T and ρ gradients, and the actual deprojected temperatures and its errors at each annulus. The errors plotted reflect only the uncertainty in the temperature in that particular bin.

The mass at the outermost point, taking into account also the uncertainties in determining both density and temperature profiles is $1.3 \pm 0.3 \times 10^{12}\ M_\odot$. The corresponding mass-to-light ratios are in the range $M/L \sim 28$–45. For M/L constant with radius, Katz & Richstone (1985) estimate $M/L \sim 15$–36 for NGC 4636, from optical velocity dispersion data and rescaled to $H_0 = 75$ km s^{-1} Mpc^{-1}, consistent with our adopted distance. Different model for the radial distribution of the dark matter led Katz & Richstone to estimate M/L ratios within the effective radius R_e as high as 180.

We do not give an estimate of the mass for the 100% cosmic abundance case. We could, as suggested earlier, interpret the multitemperature results as due to the emission of hotter, possibly isothermal gas, coexisting with cooler gas, and estimate the mass from the larger than 0.9 keV component only.

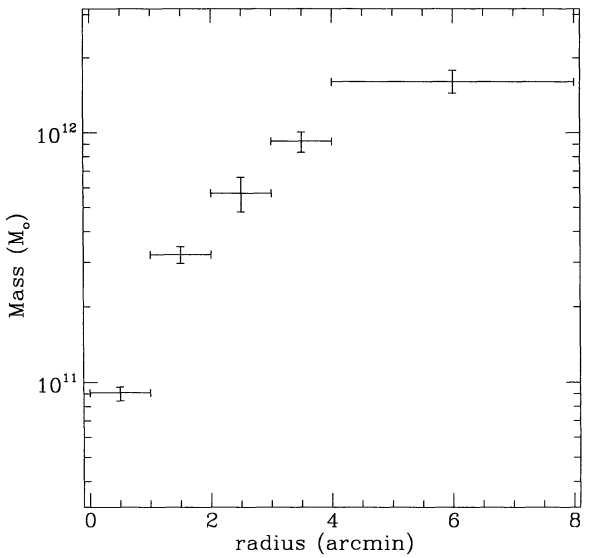

FIG. 13.—Mass distribution on the assumption of a 20% cosmic abundance model.

However, we cannot separate the spatial distribution of the different components, and we cannot therefore derive the radial density gradient, even if we were to assume a constant T. We must therefore await data that will allow us to better understand the physical nature of the gas.

9. CONCLUSIONS

A very extended source ($r \sim 18'$) is observed at and around NGC 4636. Most likely NGC 4636 itself extends out to 6′–8′, while the emission at larger radii is to be attributed to a different source. While it is unlikely that this emission has a galactic origin, whether it is the Virgo cluster that extends this far south from M87 ($\sim$3 Mpc), or whether this is a small group similar to NGC 2300 is yet to be established.

Even within NGC 4636 itself, the characteristics of the gas are as yet not completely understood. The present data indicate that either the gas is inhomogeneous, at roughly cosmic metal abundance, or the metal enrichment is very low ($\sim$20%–30% cosmic). There is however a clear temperature gradient, from $\sim$0.5 keV in the inner 1′ to 0.8–1 keV outside, regardless of the abundance percentage model adopted.

All the above ambiguities prevent us from obtaining a final estimate of the total mass of this object. Morever, the assumption of spherical symmetry, used to derive the relevant parameters (T, ρ at different radii) is not strictly valid for this galaxy, and we have neglected the possible presence of an external medium. An estimate of the total mass, derived ignoring the above objections, and for low metal abundance, gives $M(r) \sim 1.3 \pm 0.3 \times 10^{12}\ M_\odot$ for $r = 35$ kpc, $\sim$3.5 times the optical mass [if M/L(opt) = 10].

We thank R. Rampazzo and N. Caon for supplying us with data prior to publication. This work was supported by NASA grants NAG5-2049 (*ROSAT*) and NAGW-2681 (LTSA) and ASI. D. W. K. acknowledges support by the KOSEF grant 923-0200-007-2.

APPENDIX A

BACKGROUND

To quantify the significance of the low surface brightness emission, and the actual extent of the source, the background level must be known in the region covered by the source. The background templates (shown in Fig. 14 together with the galaxy's raw profile) distributed with the data by the standard processing in the three default energy bands have proved inadequate for this observation, and in general for observations with strong extended sources, mostly because at small angles they seem steeper than should be expected. This latter effect can be seen in the comparison of the radial profiles of background templates of several observations of comparable length, shown in Figure 15. All but two have a very similar shape, the two steeper cases being fields with strong extended central sources (NGC 4636 and the Pegasus I cluster). The "expected" radial distribution of a flat background, modulated by the energy-dependent vignetting, is also shown (from the exposure map), and is also significantly flatter.

We have therefore considered two different ways of predicting the background for this source: First, we might use the background template of another observation available to us, where the central source is small and therefore does not contribute to enhance significantly the background shape toward the center of the field. For this we chose an observation of similar length, made in the same period, of an object in the same region of the sky (e.g., NGC 4649), rescaled to match the count rate outside $\sim 20'$. This choice has some clear disadvantages: (1) the normalization based on the observed counts outside 20′ will most likely cancel evidences of real emission in the region; (2) a detailed analysis of features outside the round support structure might suffer, since the details of the support structure can vary from field to field (due to the telescope wobble, pointing, roll angle, etc.; however, inside $\sim 18'$ this is not a concern); (3) NGC 4649 is closer to the Virgo cluster center ($\sim 1°$) and therefore probably still well within the hot cluster emission.

Alternatively we might use the exposure map, which combines the effective exposure of each pixel (although more coarsely than the actual image) with the expected radial distribution of a flat incident component, for a given spectral model. However, since vignetting is energy dependent, while the exposure has a fixed incident spectrum, we have checked what effects we can expect for different energy bands or spectral channels. The spectral fitting routines in "PROS" provide us with the spectral distribution predicted by a given model "adjusted" to the area considered. If *all* the prarameters in the model are given, including the absolute normalization (which is equivalent to assuming that a flat component is illuminating the whole detector), then differences in the predicted count distribution at different radii reflect the vignetting correction appropriate for that particular region. We have then obtained the vignetting correction for different annuli in each spectral channel (in the 34 bin scale used by SASS and PROS) as the ratio of the predicted count distribution (obtained assuming the *same* model as described above) in the region of interest to those of a background annulus taken at 25′–27′. Figure 16 shows the ratios (i.e., the vignetting correction) for the annuli (6′–8′ and 15′–18′ relative to 25′–27′) and three different models as a function of energy channel. It is quite clear that this ratio is constant up to channel 20, while it is increases rapidly after channel 25. It is also clear that the choice of the input spectrum is basically irrelevant, in the channel range 4–30. The ratio of surface brightness in the same two annuli relative to the background region obtained from the exposure map is also plotted in the same figure, which indicates that this template can be used for most purposes, especially

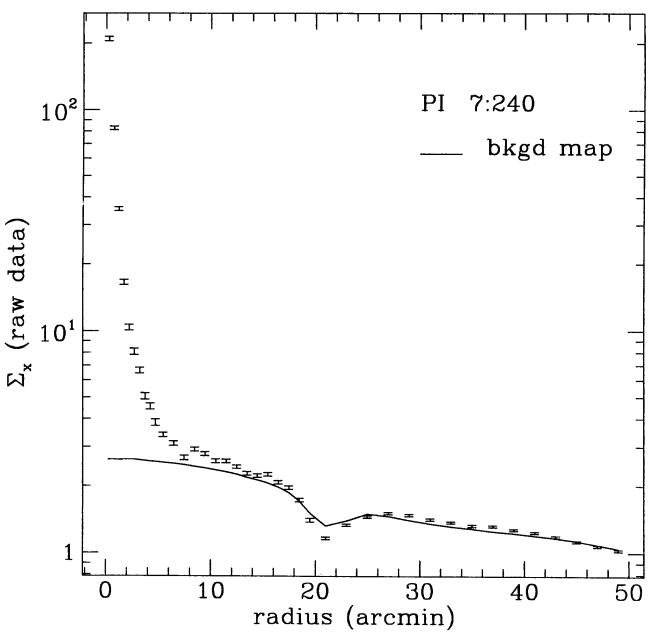

FIG. 14

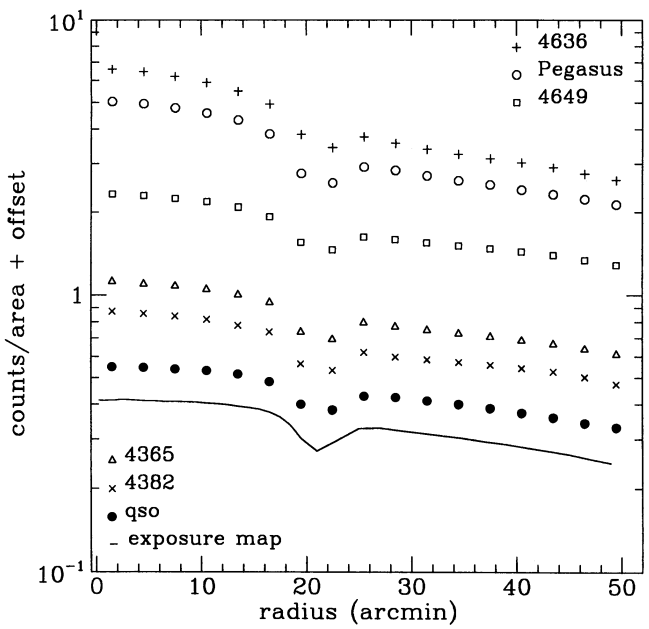

FIG. 15

FIG. 14.—Radial profile of the total raw detected counts (*points*) and the background template (*solid line*) provided by the standard software

FIG. 15.—Comparison of surface brightness profiles for several broad-band background maps, in arbitrary units. These templates correspond to observations of high Galactic latitude objects (quasars and galaxies) that do not contain very extended strong central sources (except for NGC 4636 and the Pegasus I cluster).

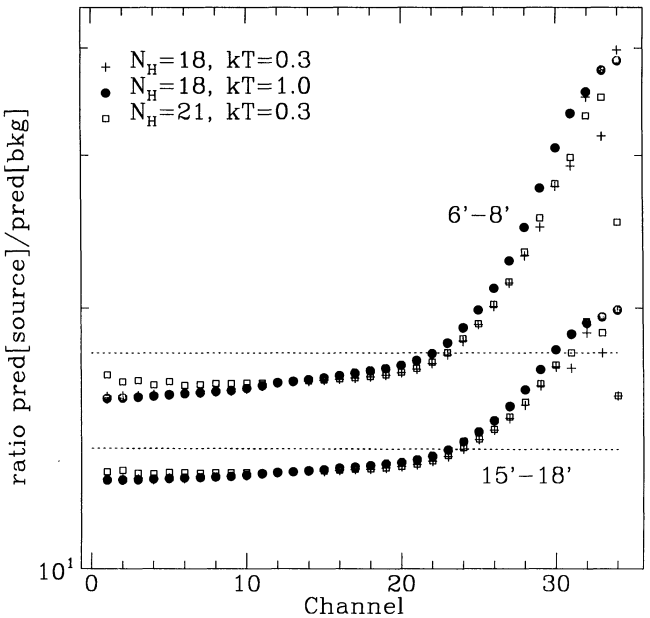

FIG. 16

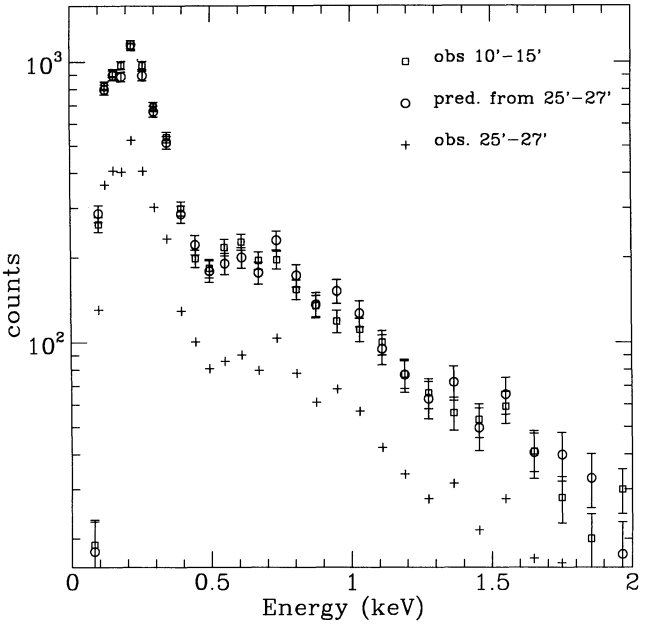

FIG. 17

FIG. 16.—Comparison of the vignetting correction that should be applied to the 25′–27′ counts to match those in the 6′–8′ and 15′–18′ regions, for three different thermal spectra, with 100% solar abundance model (Meyer 1979). Two column density values (log N_H = 18 and 21 cm^{-2}) and two temperatures (kT = 0.3 and 1 keV) are considered. The average rescale derived from the exposure map for the same regions is also plotted for comparison.

FIG. 17.—Comparison of the results of the "vignetting correction" procedure applied to background counts in the 25′–27′ region to the background count distribution in the 10′–15′ region. The observed count distribution in the 25′–27′ regions is also shown.

considering that the source count rates decrease for channel 25 and higher (we have also checked numerically the agreement on the resulting net counts).

We conclude that for spatial analysis the exposure map is a suitable background template, properly rescaled to match the emission outside 25′. This choice has also the advantage of correcting for poorly exposed region (mostly for the obscuration due to the support structure). Clearly this normalization has the same disadvantage as in the first consideration, that we are ignoring possible emission at large radii. We have confined our analysis to photons in the PHA bins 4–30, corresponding to 0.1–2.0 keV.

Although it is clear that the relative corrections in the spectral channels are small, for spectral analysis we have made full use of this technique, to correct the shape of the background, as well as the normalization. The background for each annulus is therefore obtained from the counts in the 25′–27′ annulus, normalized by area, and each spectral channel is then readjusted separately for vignetting obtained as explained above (see Fig. 16). To check that our "predictions" are indeed reproducing the spectral count distribution observed in regions free of source counts we have repeated this procedure for regions outside of 27′, and also for different observations available to us, where central sources are not as extended, so that we could check our procedure closer to the field's center. Figure 17 shows the results applied to the field of NGC 247, a normal galaxy away from the Virgo cluster emission, which confirms that our predictions are close to the observed count distribution in the 8′–15′ from a background taken at 25′–27′.

APPENDIX B

PROPERTIES OF THE SPECTRAL FITS

To reassure ourselves of the validity of our main spectral results, namely of the existence of a temperature gradient within 8′, we have investigated what changes are observed in the fitted parameters if some of the assumptions are modified. Moreover we have tried to understand what weight we should attribute to the deviations from the best-fit models observed in some channels. A comparison of the results should give a measure of the uncertainties (other than statistical) involved.

For this purpose, we have compared the results from different spectral fitting routines (PROS and XSPEC to be specific), and we have searched the range of abundance, from 20% to 300% of the cosmic value. The various metals in different models scale rigidly with the cosmic ratios. Furthermore, we have looked at the time history of the observation.

Abundance.—Table 7 shows the (PROS) best-fit parameters for a two-temperature fit for each annulus, for a range of abundance models. Notice that the PROS software allows us to use only discrete values of the abundance percentages. The XSPEC software could be used instead for continuous values, however, given the different assumption for the Fe abundance in XSPEC (see later), and our conclusions that a *measure* of the abundance is not yet possible with the present data, we have completed the test using PROS consistently.

The results of Table 7 indicate a rather complex situation. The best-fit values would indicate that low abundances are preferred at the center, while roughly cosmic values are suggested for the 2′–6′ region. Otherwise, all models give equivalent "goodness of fit"

TABLE 7

COMPARISON OF THE BEST-FIT PARAMETERS FROM A THIN THERMAL PLASMA (RAYMOND CODE), TWO-TEMPERATURE SPECTRUM, FOR DIFFERENT COSMIC ABUNDANCE PERCENTAGES

Annulus	Channel	N_H	kT_1	Norm[a]	kT_2	Abundance	χ^2
0′–1′	[4:29]	20.45	0.557	−1.00	0.729	20%	24
1′–2′	[4:29]	20.43	0.685	−1.00	0.698	20	16
2′–3′	[4:28]	20.43	0.753	−1.00	0.737	20	39
3′–4′	[4:28]	20.46	0.799	−1.00	0.849	20	28
4′–6′	[5:27]	20.35	0.848	−0.88	0.824	20	33
6′–8′	[4:26]	20.05	0.776	−0.96	0.835	20	9
8′–10′.....	[4:29]	19.90	0.667	−0.14	2.885	20	15
10′–12′.....	[5:27]	19.88	0.770	−0.14	1.534	20	16
12′–15′.....	[4:27]	19.94	0.685	0.01	2.891	20	26
15′–18′.....	[5:26]	19.88	0.953	−0.01	0.961	20	20
0′–1′	[4:29]	20.35	0.588	−1.00	0.556	30	32
1′–2′	[4:29]	20.34	0.684	−1.00	2.999	30	15
2′–3′	[4:28]	20.33	0.768	−0.86	0.767	30	29
3′–4′	[4:28]	20.38	0.830	−0.98	0.813	30	21
4′–6′	[5:27]	20.25	0.862	−0.97	0.862	30	26
6′–8′	[4:26]	19.88	0.806	−0.97	0.787	30	9
8′–10′.....	[4:29]	19.75	0.647	0.08	2.874	30	16
10′–12′.....	[5:27]	19.74	0.705	0.22	1.374	30	16
12′–15′.....	[4:27]	19.81	0.674	0.19	2.898	30	25
15′–18′.....	[5:26]	19.66	0.969	−0.22	0.968	30	19
0′–1′	[4:29]	20.29	0.570	−1.00	2.900	40	34
1′–2′	[4:29]	20.28	0.667	−0.55	2.898	40	15
2′–3′	[4:28]	20.26	0.765	−1.00	2.900	40	26
3′–4′	[4:28]	20.31	0.843	−0.94	0.821	40	17
4′–6′	[5:27]	20.16	0.862	−0.62	0.871	40	24
6′–8′	[4:26]	19.74	0.791	−0.77	1.378	40	9
8′–10′.....	[4:29]	19.64	0.633	0.22	2.837	40	16
10′–12′.....	[5:27]	19.61	0.621	0.45	1.275	40	17
12′–15′.....	[4:27]	19.72	0.662	0.32	2.899	40	25
15′–18′.....	[5:26]	19.41	0.966	−1.00	2.889	40	19
0′–1′	[4:29]	20.28	0.535	−0.46	2.900	50	32
1′–2′	[4:29]	20.23	0.660	−0.38	2.618	50	15
2′–3′	[4:28]	20.18	0.768	−1.00	2.900	50	23
3′–4′	[4:28]	20.24	0.857	−0.27	0.829	50	16
4′–6′	[5:27]	20.08	0.872	−0.44	0.884	50	23
6′–8′	[4:26]	19.64	0.778	−0.46	1.739	50	10
8′–10′.....	[4:29]	19.55	0.622	0.32	2.887	50	17
10′–12′.....	[5:27]	19.45	0.659	0.42	1.559	50	17
12′–15′.....	[4:27]	19.64	0.650	0.42	2.899	50	25
15′–18′.....	[5:26]	19.09	0.889	0.12	1.159	50	19
0′–1′	[4:29]	20.29	0.462	−0.27	0.995	60	33
1′–2′	[4:29]	20.20	0.654	−0.26	2.550	60	16
2′–3′	[4:28]	20.12	0.768	−0.86	2.900	60	22
3′–4′	[4:28]	20.18	0.851	−0.59	0.852	60	15
4′–6′	[5:27]	20.00	0.873	−0.94	0.966	60	22
6′–8′	[4:26]	19.54	0.764	−0.25	1.934	60	11
8′–10′.....	[4:29]	19.49	0.595	0.41	2.896	60	17
10′–12′.....	[5:27]	19.30	0.656	0.48	1.719	60	17
12′–15′.....	[4:27]	19.56	0.643	0.50	2.879	60	25
15′–18′.....	[5:26]	19.00	0.927	−0.11	2.880	60	19
0′–1′	[4:29]	20.73	0.624	0.20	0.111	70	29
1′–2′	[4:29]	20.16	0.651	−0.18	2.797	70	17
2′–3′	[4:28]	20.06	0.768	−0.71	2.900	70	21
3′–4′	[4:28]	20.13	0.854	−0.43	0.853	70	15
4′–6′	[5:27]	19.92	0.880	−0.36	0.902	70	22
6′–8′	[4:26]	19.45	0.757	−0.14	2.144	70	11
8′–10′.....	[4:29]	19.41	0.584	0.47	2.897	70	17
10′–12′.....	[5:27]	19.13	0.658	0.53	1.928	70	18
12′–15′.....	[4:27]	19.49	0.635	0.54	2.868	70	25
15′–18′.....	[5:26]	19.00	0.905	0.12	2.890	70	20
0′–1′	[4:29]	20.19	0.459	−0.20	1.125	100	39
1′–2′	[4:29]	20.08	0.641	−0.01	2.708	100	18
2′–3′	[4:28]	19.93	0.764	−0.42	2.899	100	19
3′–4′	[4:28]	20.02	0.845	−0.71	2.898	100	15
4′–6′	[5:27]	19.70	0.868	−0.08	0.933	100	22
6′–8′	[4:26]	19.23	0.743	0.11	2.729	100	12
8′–10′.....	[4:29]	19.20	0.561	0.59	2.898	100	18

TABLE 7—*Continued*

Annulus	Channel	N_H	kT_1	Norm[a]	kT_2	Abundance	χ^2
10′–12′.....	[5:27]	19.00	0.346	0.54	1.150	100	18
12′–15′.....	[4:27]	19.27	0.618	0.67	2.899	100	25
15′–18′.....	[5:26]	19.00	0.855	0.49	2.899	100	21
0′–1′	[4:29]	20.04	0.497	0.11	2.878	200	50
1′–2′	[4:29]	19.91	0.623	0.26	2.900	200	22
2′–3′	[4:28]	19.67	0.750	−0.04	2.900	200	18
3′–4′	[4:28]	19.80	0.828	−0.13	2.896	200	15
4′–6′	[5:27]	19.33	0.860	−0.14	2.895	200	23
6′–8′	[4:26]	19.00	0.693	0.52	2.900	200	15
8′–10′.....	[4:29]	19.00	0.418	0.68	2.398	200	20
10′–12′.....	[5:27]	19.01	0.267	0.49	1.124	200	18
12′–15′.....	[4:27]	19.01	0.346	0.51	1.301	200	26
15′–18′.....	[5:26]	19.00	0.217	0.64	1.083	200	18

[a] Log of the ratio of the second component normalization relative to the first component [i.e., log (*N*2/*N*1)].

and in any case the best-fit low temperature kT_1 is virtually unaffected by the choice of cosmic abundance percentages. As the value of kT_2 is usually poorly determined, similarities here are hardly significant.

The assumption of the solar abundance model (Meyer 1979) does not change significantly the results: the best-fit values are consistent with those in the cosmic abundance case, and there is a similar trend of increasing kT_1 (at the best-fit value) with radius.

Although the metal abundance can be very low, we can exclude a thermal bremsstrahlung model with no lines (i.e., exponential model times (Gaunt factor), which gives unacceptable high values of χ^2. For the inner 1′ circle, $\chi^2_{\rm min} = 938$ for one-temperature model, and this value is not reduced by the addition of more temperature components.

Time history—The observation was carried out in eight time intervals (OBI), over the period 24–26 1991 December. The time intervals (with the exception of the fourth, <100 s long) range from 1500–3500 s, and end when the satellite orbit enters the South Atlantic Anomaly (SAA). We have looked at the overall count rate in each OBI and found that they all behave well, that is, no significant increase in the overall count rate is observed except at the end, where the SAA enhances the count rate very rapidly, before the "accepted data interval" ends. We have then obtained the spectral count distribution using only "best" data (i.e., truncating the accepted observing times so as to minimize or exclude the contribution from the SAA) and checked that the results are consistent with those obtained with all the data. Table 8 shows an example for the 2′–3′ region, for 20% and 100% cosmic abundance models.

Significance of the parameters.—The 90% confidence region has been derived for the interesting parameters, as listed in the relevant tables. We have also analyzed the significance of the second temperature value, for the two-temperature fits, and its relative strength. Figure 18 shows the χ^2 grid for two interesting parameters (kT_1 and kT_2), for the two inner annuli. The N_H is allowed to vary around the line-of-sight value. All values of $kT_2 > 1$ are acceptable, and it is not possible to measure it better with these data. At the same time the normalization of the second component can vary between 30% and 100% of the first normalization in the innermost annulus, and from 50 to greater than 100% in the 1′–2′ region. Similarly, the second temperature for the fits outside 8′ is not well constrained, but is $kT_2 > 0.8$ keV.

We have also evaluated how much the background rescaling values influence the results. As shown in § 2.5, the determination of temperatures is very solid regardless of where we obtain the background counts. This is also true if we use different rescaling factors applied to the counts in the 25′–27′ region. The determination of N_H however is somewhat affected by the rescaling values (see also § 2.5).

XSPEC vs. PROS.—A last check was done that compares the results obtained from the PROS and the XSPEC softwares. We found that qualitatively the two systems give consistent results, that is, they agree as to where a minimum of a given spectral model is. There are, however, differences in the value of χ^2 in some of the models tried, that result from different predicted models. After a few systematic comparisons of the predicted models from the two softwares, we believe that the reason for the differences are due to the following:

PROS currently has a later version of the "Raymond" code.

In spite of the same name "cosmic abundance," the assumed ratios for the heavy elements relative to hydrogen are not the same. Ratios are the same for all elements except Fe and are the Allen (1973) values. In PROS, Fe is consistently taken from Allen; in

TABLE 8

COMPARISON OF BEST-FIT PARAMETERS FOR THE 2′–3′ ANNULUS, USING ALL DATA AND "BEST" DATA

Counts	Error	N_H	90% Region	kT	90% Region	χ^2	Model (cosmic)	Data Set
1279.5.....	39	20.43	20.30–20.50	0.767	0.70–0.80	45.7	20%	"Best"
		19.87	19.65–20.10	0.806	0.75–0.85	27.2	100	"Best"
1732.6.....	47	20.43	20.35–20.50	0.751	0.70–0.79	39.4	20	"All"
		19.84	19.70–20.05	0.795	0.75–0.84	21.1	100	"All"

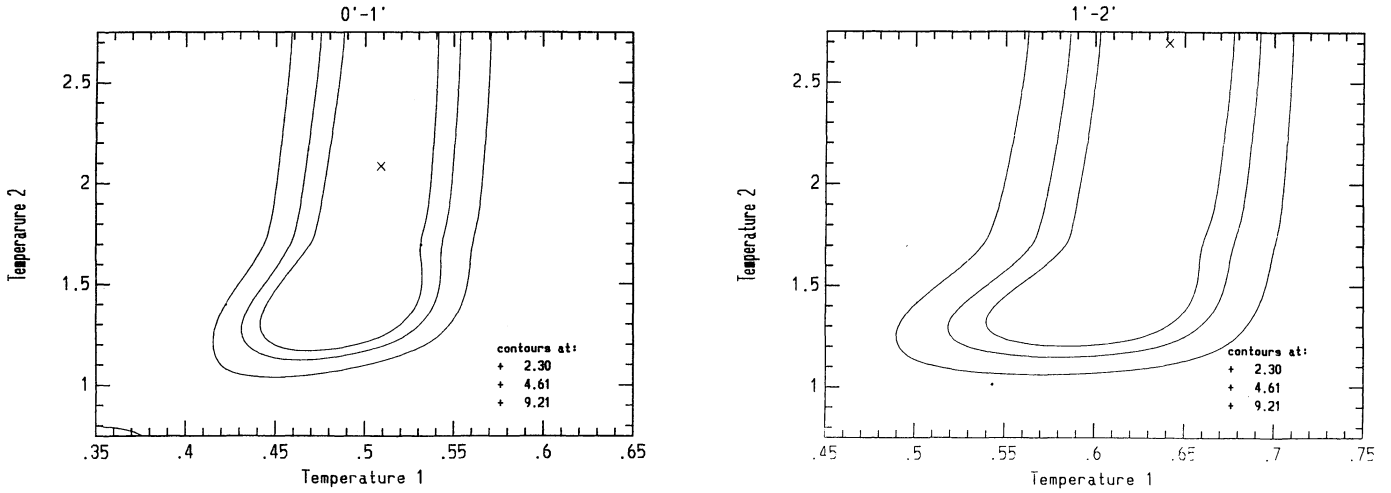

FIG. 18.—Confidence contours for kT_1 and kT_2, for a two-temperature spectrum, with 100% cosmic abundances. The N_H and the relative normalization of the second component are let free to vary.

XSPEC, the solar value from Ross & Aller (1976) is used. Taking advantage of the flexibility of the XSPEC software, it is possible to use the same abundance ratios for all elements (model vraymond). The comparison between the PROS and XSPEC models thus obtained indicates that the different choice of standard abundance ratios, rather than the different version of the "Raymond" code, probably gives the bigger effect of the two, although this is somewhat dependent of the temperature assumed for the model.

The effect of absorption is different in the two softwares, even though both are derived from Morrison & McCammon (1983).

An example of the difference in the predicted models is shown in Figure 19, for the innermost 1′ region. We have used the best-fit, two-temperature model (cf. Fig. 9*b*) with the following parameters: $N_H = 7.4 \times 10^{20}$ cm^{-2}; $kT_1 = 0.08$ keV; $kT_2 = 0.60$; 100% cosmic abundance. In XSPEC, we have used the default Raymond model. The χ^2 differ by ~ 8 for the same model parameters (see Fig. 19). Since this is true only for some of the models, while in others the agreement is much better, some quantitative differences

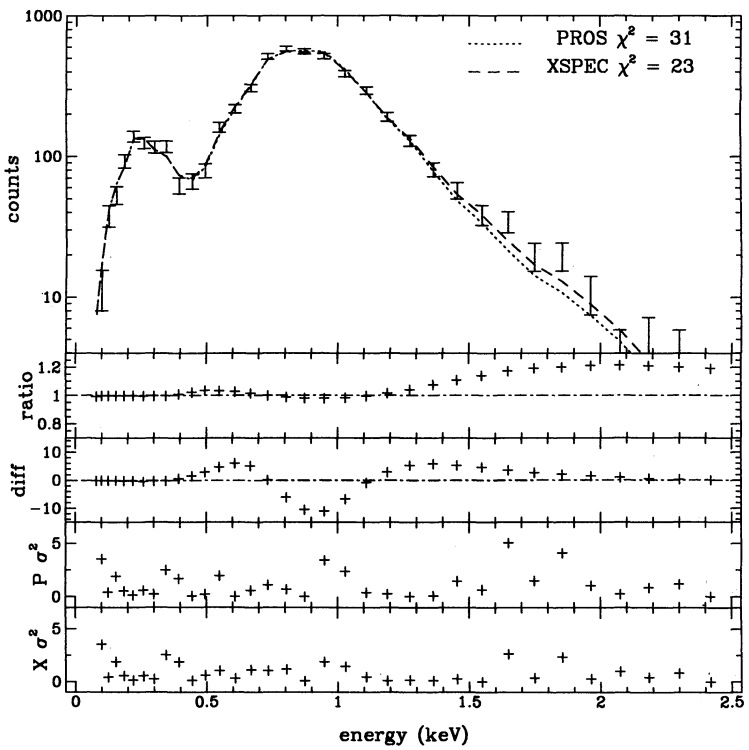

FIG. 19.—Comparison of the spectral models predicted by the PROS and the XSPEC softwares. In both cases the qualitative agreement with the data is good, but small differences are observed mostly for energies above 1.5 keV. The different panels are, from top to bottom: comparison between the observed counts (0′–1′) with the models; ratio of the XSPEC to PROS model; difference XSPEC predicted counts – PROS predicted counts; ([observed—predicted]/error)^2 for PROS; ([observed – predicted]/error)^2 for XSPEC.

arise in the search for the confidence contours. For example, to derive the range of abundance allowed by the fit, the PROS software would formally exclude the 100% abundance model while XSPEC accepts up to 100% abundances (however, see the above discussion on the difference in abundance ratios). This clearly adds uncertainties in the search of the confidence region, in particular for abundance percentages, since this parameter is probably more model dependent than others.

REFERENCES

Allen, C. W. 1973, Astrophysical Quantities (New York: Athlone Press)
Awaki, H., Koyama, K., Kunieda, H., Takano, S., Tawara, Y., & Ohashi, T. 1991, ApJ, 366, 88
Bertin, G., Pignatelli, E., & Saglia, R. P. 1993, A&A, 271, 381
Cowie, L. L., & Binney, J. 1977, ApJ, 215, 723
De Vaucouleur, G., de Vaucouleur, A., Corwin, G. C., Jr., Buta, R. J., Paturel, G., & Fouqué, P. 1991, Third Reference Catalog of Bright Galaxies (Berlin: Springer)
Fabbiano, G. 1989, ARA&A, 27, 87
Fabian, A. C., Thomas, P. A., Fall, S. M., & White R. E., III 1986, MNRAS, 221, 1049
Fabricant, D., & Gorenstein, P. 1983, ApJ, 267, 535
Forman, W., Jones, C., & Tucker, W. 1985, ApJ, 293, 102
Forman, W., Schwarz, J., Jones, C., Liller, W., & Fabian, A. C. 1979, ApJ, 234, L27
Gaetz, T. J. 1985, Ph.D. thesis, Cornell Univ.
Katz, N., & Richstone, D. O. 1985, ApJ, 296, 331
Kim, D.-W., Fabbiano, G., & Trichieri, G. 1992, ApJ, 393, 134
Kriss, G. A., Cioffi, D. F., & Canizares, C. R. 1983, ApJ, 272, 439
Meyer, J. P. 1979, in Comm. 22d Colloq. Internat. d'Astrophysique, Liége, Les Eléments et Leurs Isotopes dans l'Univers, 153
Morrison, R., & McCammon, D. 1983, ApJ, 270, 119
Mulchaey, J. S., Davis, D. S., Mushotzky, R. F., & Burstein, D. 1993, ApJ, 404, L9
Pfeffermann, E., et al. 1987, Proc. SPIE, 733, 519
Ross, J. E., & Aller, L. H. 1976, Science, 191, 1223
Stark, A. A., Gammie, C. F., Wilson, R. W., Bally, J., Linke, R. A., Heiles, C., & Hurwitz, M. 1992, ApJS, 79, 77
Trinchieri, G., Fabbiano, G., & Canizares, C. R. C. 1986, ApJ, 310, 637 (TFC)
Truemper, J. 1983, Adv. Space Res., 2, 241
Tully, B. 1988, Nearby Galaxy Catalog (Cambridge: Cambridge Univ. Press)
Vedder, P. W., Trester, J. J., & Canizares, C. R. 1988, ApJ, 332, 725
Zwicky, F., Herzog, E., Karpowicz, M., Kowal, C., & Wild, P. 1961–1968, Catalogue of Galaxies and of Cluster of Galaxies (Pasadena: California Institute of Technology)